Natural Hazards
and Earth System
Sciences

Open Access

Mesoscale numerical simulations of heavy nocturnal rainbands associated with coastal fronts in the Mediterranean Basin

J. Mazon[1] **and D. Pino**[1,2]

[1]Department of Applied Physics, Universitat Politècnica de Catalunya BarcelonaTech (UPC), Barcelona, Spain
[2]Institute for Space Studies of Catalonia (IEEC-UPC), Barcelona, Spain

Correspondence to: J. Mazon (jordi.mazon@upc.edu)

Abstract. Three offshore rainbands associated with nocturnal coastal fronts formed near the Israeli coastline, the Gulf of Genoa and on the northeastern coast of the Iberian Peninsula, are simulated using version 3.3 of the WRF-ARW mesoscale model in order to study the dynamics of the atmosphere in each case.

The simulations show coastal fronts producing relatively high (in comparison with some other similar rainbands) 1 and 10 h accumulated precipitations that formed in the Mediterranean Basin. According to these simulations, the coastal fronts that formed near the Israeli coastline and over the Gulf of Genoa are quasi-stationary, while the one that formed on the northeastern coast of the Iberian Peninsula moves away from the coast. For the three events, we evaluate and intercompare some parameters related to convective triggering, deceleration induced by the cold pool in the upstream flow, and the blockage that the cold coastal front offers to the warmer maritime air mass.

1 Introduction

When drainage winds interact with a prevailing flow, nocturnal offshore rainbands can form close to the coastline. This is a commonly observed phenomena during the night and early morning in many areas of the world, especially in the tropics. The physical mechanism producing offshore rainbands is well known. After sunset, the inland air cools more quickly and moves towards the coastline along the riverbeds and slopes of the mountains located near the coast. This cold air mass moves offshore as a density current and can form a coastal front when it reaches the sea and interacts with a warmer and moister maritime air mass. As a consequence, the warmer and moister sea air is lifted over the cold front. When ascending, it may condensate and form stratiform clouds if it reaches the lifting condensation level (LCL). In some cases, convective clouds eventually appear if the level of free convection (LFC) is reached. In any case, the depth of the colder inland air mass (H) plays an important role in helping the moister and warmer maritime air mass reach LCL or LFC (Schoenberg, 1984; Miglietta and Rotunno, 2010). The latter authors conducted idealized numerical studies of the triggering mechanisms which enhance forced nocturnal convection due to orography. They concluded that moderate precipitation occurs if the height of the mountain, h, is located near or above the LFC. In contrast, stratiform clouds, which produce weak or no precipitation, form if h is approximately equal to or higher than the LCL, but lower than the LFC; if h is lower than the LCL, clear skies prevail. Miglietta and Rotunno (2010) defined some other parameters to explain the intensity and the location of convective rainfall over idealized mountains, such as the triggering parameter $h/$LFC. Values greater than 1 of this parameter suggest that convective cells appear over the mountain, while smaller values indicate that convection is inhibited. NLFC$/U$ is another proposed parameter that measures the deceleration induced by the convective cold pool on the upstream flow, where N is the Brunt–Väisälä frequency and U is the horizontal wind speed of the flow blowing perpendicular to the mountain.

Moreover, Durran and Klemp (1987) defined the parameter Nh/U, which accounts for the blockage that a mountain causes on a prevailing flow. They found that for $Nh/U \approx 0.25$, the air flows easily over a mountain ridge with little blockage and minor decelerations on the upwind side

of the ridge. For $Nh/U \approx 5$, the flow is entirely blocked by the mountain, and the air is either forced upwards with high vertical accelerations or horizontally around the ridge.

As a first approach, it can be assumed that the cool pool associated with a coastal front acts as a mountain range that blocks, lifts and decelerates the prevailing warmer flow. The observed and simulated nocturnal coastal fronts are relatively large offshore convergence lines that separate a cold air mass (inland drained air) from a warmer maritime air (sea air). Since these two air masses have different densities they do not mix, and consequently the maritime air mass is lifted mainly over the cold one. Then, the triggering parameter h/LFC (proposed and defined by Miglietta and Rotunno, 2010) can be rewritten as H/LFC. It is important to note that while h and the LFC defined by Miglietta and Rotunno (2010) are related to a single air mass, in our case H is related to the height of the cool pool associated with the cold coastal front, with the LFC belonging to the warm, moist and unstable maritime air mass. In the same way, the blockage parameter defined in Durran and Klemp (1987) is redefined as NH/U, where U is the relative wind speed of the two air masses. Finally, using the WRF-ARW mesoscale model (Skamarock et al., 2008) results, we define the coastal-front depth (H) as the maximum height where a large enough horizontal gradient of potential temperature is present. This is estimated by plotting a vertical cross section of the simulated potential temperature along a line perpendicular to the coastline.

Several authors have studied nocturnal fronts at tropical coastlines. Yu and Jou (2004) detected and studied the formation of thunderstorms off the southeast coast of Taiwan, finding that they are associated with rainbands that occur daily and regularly. Houze et al. (1981) used radar data to study the effect of wind cycles and the associated rainfall in Borneo, including nocturnal offshore rainbands. These authors concluded that land breeze enhances convection offshore, and consequently rainbands. Mori et al. (2004) described the formation of convective systems generated by offshore winds off the coast of Sumatra, which move away from the coast during the night at speeds of around $10\,\mathrm{km\,h^{-1}}$. Murakami (1983) described a front caused by drainage winds during the winter months on the southeast coast of Japan, thus producing an increase in rainfall as compared to other nearby areas. Lau and Yi-Leng (1999) analyzed radio soundings to describe the nocturnal rainfall in certain regions in Hawaii, attributing it to the formation of a front caused by nocturnal drainage winds. Frye and Chen (2001) studied the evolution of intense drainage winds that generated showers at night, also on the island of Hawaii, finding that intense drainage winds of up to $11\,\mathrm{m\,s^{-1}}$ generate showers at night. Ohsawa et al. (2003) used satellite images to analyze nocturnal precipitation caused by nocturnal fronts over Bangladesh, Thailand, Vietnam and Malaysia, attributing this precipitation to nocturnal katabatic winds. Mapes et al. (2003) used the MM5 model to describe and model the rain on the western coast

of Panama and Colombia. They found that the diurnal cycle of overland precipitation between August and September has an afternoon maximum caused by convective systems. Moreover, there is a nocturnal maximum of precipitation over the valleys of the Andes and Lake Maracaibo, as well as on the Pacific coast during the night and early morning. This nocturnal maximum propagates offshore as the day progresses. Wu et al. (2008), used the TRMM satellite to detect offshore rainfall during the night and early morning in West Kalimantan (Indonesia), which was caused by strong offshore flow (land breezes). Wapler and Lane (2012) used the WRF-ARW mesoscale model to study the nocturnal offshore convection near Darwin (Australia), finding that the interaction between land breeze and synoptic flow causes nocturnal convection over this area.

Despite the large number of references dealing with rainbands associated with nocturnal coastal fronts, there are only a few studies focusing on nocturnal rainbands over the Mediterranean Basin. Probably the most iconic investigation of nocturnal coastal fronts in this basin was made by Neumann (1951). This author proposed a convergence between a prevailing synoptic wind and the land breeze to explain the observed offshore convection in south Israel. Goldreich et al. (2004) describe local nocturnal precipitation from September to November in south Israel, which is produced by a coastal front near the coastline and formed by a land breeze interacting with a synoptic flow, thus contributing significantly to the total amount of rainfall in this area during dry years. In the same area, Heiblum et al. (2011) suggest that the concave shape of the coastline plays an important role in enhancing the convergence of the land breeze and synoptic winds near the coastline, with a significant effect on the precipitation in south Israel. Furthermore, Mazon and Pino (2013b) used the WRF-ARW mesoscale model to simulate several nocturnal coastal fronts on the coasts of Israel, Italy and Libya, focusing on the role of the large sea–land thermal difference, the sea surface temperature and the shape of the coastline.

In the western Mediterranean Basin, Callado and Pascual (2002) detected nocturnal convection at the mouths of three rivers that flow into the northeastern coast of the Iberian Peninsula. Mazon and Pino (2009) studied the increase in nocturnal precipitation at the mouth of the Llobregat River (close to Barcelona city), which is caused by the interaction between the relatively cold drainage winds and the warm and moist Mediterranean air mass, especially during late summer and early autumn. Mazon and Pino (2013a) used the MM5 mesoscale model (Grell et al., 1994) to simulate two nocturnal coastal fronts in the south and northeast of the Iberian Peninsula.

Here we numerically investigate three observed events of relatively intense precipitation associated with nocturnal cold coastal fronts that formed near the coast in some areas of the Mediterranean Basin, which were caused by the drainage of cold inland air interacting with a prevailing
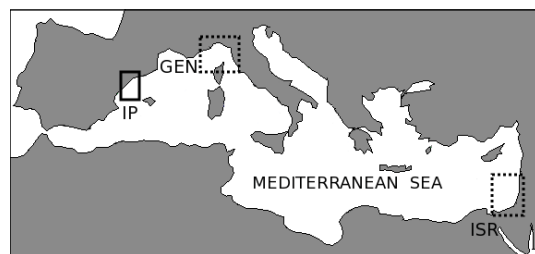
Figure 1. Location of the nocturnal coastal fronts that affected the Israeli coast (ISR) on 6 January 2011, the Gulf of Genoa (GEN) on 30 January 2008, and the northeastern coast of the Iberian Peninsula (IP) on 6 September 2011. Rectangles correspond approximately to the smallest domains used in each of the WRF-ARW simulations. Dashed rectangles indicate quasi-stationary fronts, while the closed rectangle indicates a non-stationary coastal front.

Table 1. Start and run times, nested domains, and the location of the largest domains used for each event in the WRF-ARW simulation.

Event	Date start (00:00 UTC)	Running times (h)	Horizontal domain resolution (km)	Center of largest domain
ISR	4 January 2011	90	27, 9, 3, 1	32.1° N–34.8° E
GEN	28 January 2008	90	18, 6, 2	44° N–9° E
IP	6 September 2011	72	18, 6, 2	41.9° N–2.07° E

warmer and moister air mass. We seek to contribute to a better understanding of this regional phenomenon over the Mediterranean Basin. For this purpose, we have selected three nocturnal coastal fronts that are associated with relatively high 1 and 10 h accumulated precipitation (which is relatively high in respect to some other studied events in the Mediterranean Basin), and we have simulated them by using the WRF-ARW mesoscale model (Skamarock et al., 2008). The first selected event (ISR) occurred on the southern coast of Israel on 6 January 2011; it has already been described by Mazon and Pino (2013b). The second event (GEN) occurred in the Gulf of Genoa on 30 January 2008, and the third selected event (IP) on the northeastern coast of the Iberian Peninsula on 6 September 2011. Figure 1 shows the location of these events within the Mediterranean Basin.

The structure of this paper is as follows. Section 2 is devoted to describing the methodology used in this investigation. Section 3 focuses on the observational data of the investigated rainbands. Section 4 shows the results of the simulations, with a focus on the analysis of the ISR, GEN and IP events. The paper ends with Sect. 5, where the conclusions are presented.

2 Methodology

To detect and analyze nocturnal rainbands in the Mediterranean Basin, we used three steps to define the methodology. First, nocturnal rainbands were detected with the Tropical Radar Measurement Mission (TRMM) Multisatellite Precipitation Analysis (TMPA) data (Haddad et al., 1997; Huffman et al., 2007). The multisatellite uses an algorithm to estimate precipitation occurring within the global latitude belt 50° N–50° S though an algorithm (Huffman et al., 2007). Product 3B42 V7 provided 3-hourly rainfall estimations at a spatial resolution of 0.25°. TRMM data was analyzed from 18:00 UTC to 09:00 UTC in several Mediterranean areas in order to detect possible nocturnal precipitation events. To accept that

the events detected by TRMM have been caused by nocturnal drainage winds or a land breeze interacting with a synoptic flow, the following conditions had to be fulfilled: (i) the nocturnal precipitation formed near the coastline; (ii) the precipitation spot either remained quasi-stationary offshore near the coast, or it moved slightly; (iii) it lasted no more than 6 consecutive hours, and disappeared a few hours after sunrise; and finally, (iv) it extended no more than 500 km, being sometimes in clusters of several individual cells.

From January 2008 to December 2012, around 50 cases were observed by analyzing the TRMM database. It is important to note that, at the latitudes where the events occurred, the TRMM does not record but estimates the accumulated precipitation. For this reason, the precipitation estimated by the TRMM has to be used with caution when validating the amount of precipitation simulated by any mesoscale model.

The second step consisted of analyzing the synoptic situation of the selected events. By doing so, we discarded those events whereby precipitation was likely caused by other atmospheric mechanisms, such as low pressure areas or large-scale fronts. For this step, we used the NCEP reanalysis database at sea level and 850 hPa (available on http://www.wetterzentrale.de/topkarten/fsreaeur.html).

Finally, for the third step, we used version 3.3 of the Advanced Research WRF-ARW mesoscale model to simulate the events whose precipitation is not associated with the kinds of meteorological disturbances mentioned above, but rather, were more likely due to a coastal front. Among the 50 potential events selected from the database, 15 were analyzed by using NCEP reanalysis and simulated with WRF-ARW. Here we investigated in detail the 3 events whose rainbands had the largest amount of precipitation.

The WRF-ARW vertical configuration for all the studied events includes 42 σ-vertical levels. The number of nested domains we used is shown in Table 1, along with other relevant information about the domains. The same physical schemes were used for all the numerical simulations performed. The MRF scheme was used for the PBL parameterization (Hong and Pan, 1996); the RRTM scheme for longwave radiation (Mlawer et al., 1997); the MM5 shortwave scheme for shortwave radiation (Dudhia, 1989); and the WSM scheme for the microphysics parameterization (Hong et al., 2004). No cumulus parameterization was used for
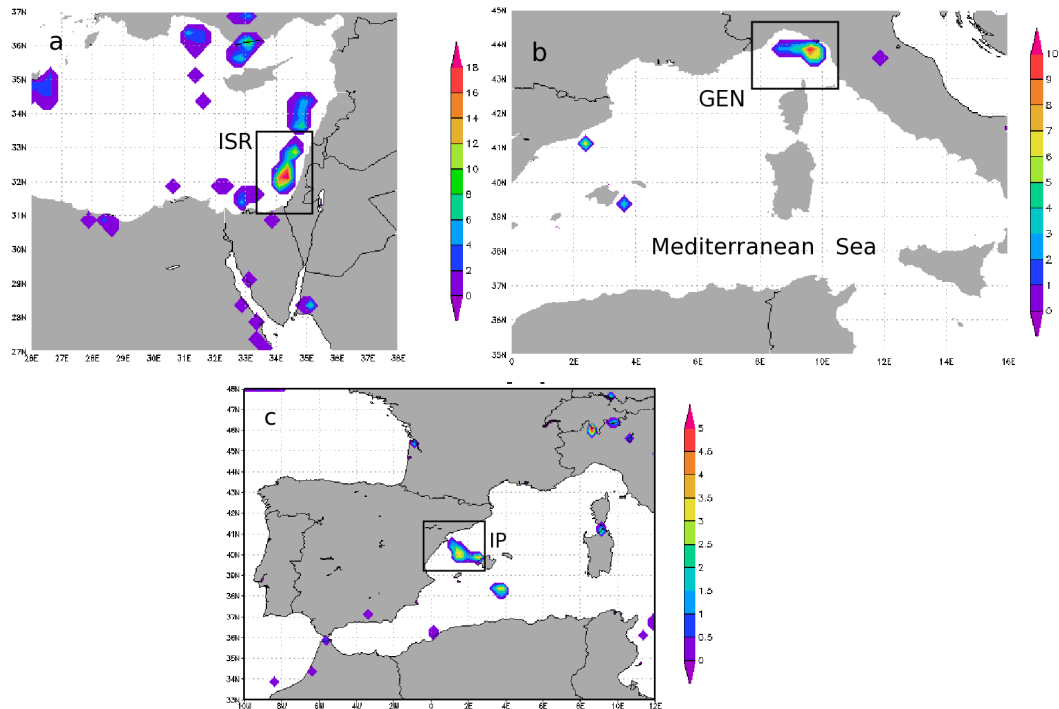
Figure 2. 3 h accumulated precipitation estimated by TRMM between **(a)** 00:00 and 03:00 UTC on 6 January 2011 for the ISR event, **(b)** 03:00 and 06:00 UTC on 30 January 2008 for the GEN event, and **(c)** 03:00 and 06:00 UTC on 6 September 2011 for the IP event. The solid rectangle indicates the approximate location of the domain used in the WRF simulation.

the smallest domains because the horizontal resolution was higher than 3 km. The initial and boundary conditions (the latter updated every 6 h) were obtained from the ECMWF operational model analysis at 0.125° horizontal resolution.

3 Observations

Figure 2 shows the 3 h accumulated rainfall, according to TRMM estimation, for the (a) ISR event from 00:00 to 03:00 UTC, (b) GEN event from 03:00 to 06:00 UTC and (c) IP event from 03:00 to 06:00 UTC. No precipitation was estimated by TRMM 3 h before or after the times of the GEN and ISR events. For the IP event, a few small precipitation cells were estimated between 03:00 to 06:00 UTC (not shown).

Reflectivity radar and/or Meteosat satellite images were also used, when available, to validate the simulations. Figure 3a and b show the reflectivity radar image of the IP event, which was obtained from the Spanish Meteorology Agency (AEMET) and the Meteosat satellite image in the mid-IR channel (3.48–4.36 μm) at 03:00 UTC, respectively. An offshore rainband near the coast was recorded by both instruments. Figure 3c shows the Meteosat satellite image of the ISR event in the mid-IR channel at 06:00 UTC. The radar reflectivity images from 03:00 to 09:00 UTC are shown in Fig. 1 of Heiblum et al. (2011). Both instruments recorded

a rainband formed by several cells near the coast offshore. Figure 3d shows the NOAA-18 image recorded in the thermal IR channel (10.3–12.5 μm) at 02:32 UTC on 30 January 2008, where clouds over the Gulf of Genoa can be observed. For this event, no radar reflectivity images were available.

4 Results

4.1 10 h accumulated precipitation

Figure 4 shows the simulated 10 h accumulated precipitation and the surface wind field at 10:00 UTC for the (a) ISR, (b) GEN and (c) IP events. In all three cases, an offshore rainband was simulated near the coastline, producing significant amounts of precipitation when compared with other simulated events in the Mediterranean Basin (Mazon and Pino, 2013a, b). The simulated rainbands were located at approximately the same position as those estimated by the TRMM, or recorded by radar. They also correspond to the clouds observed by Meteosat (see Figs. 2 and 3).

The rainband observed in the ISR event has been already studied by Mazon and Pino (2013b), but not the 10 h accumulated precipitation. As described in Mazon and Pino (2013b), this line of precipitation is quasi-stationary as a consequence of a strong drainage wind, with wind speed similar to the
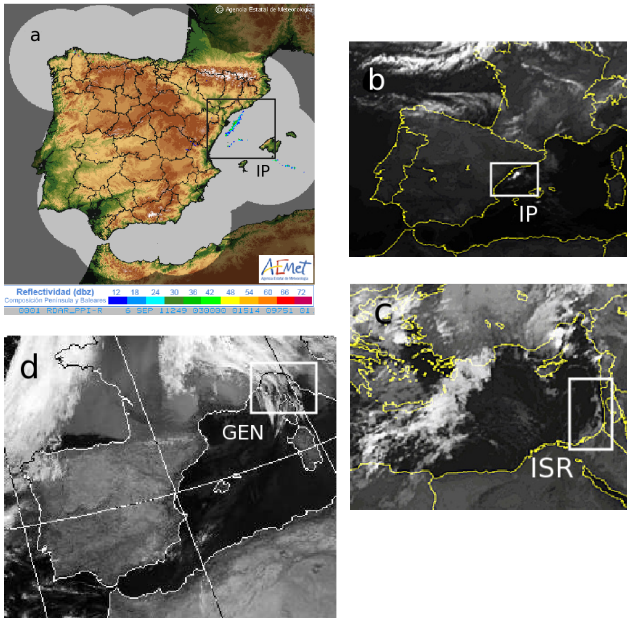
Figure 3. Data recorded from **(a)** the reflectivity radar image at 03:00 UTC on 6 September 2011, **(b)** the Meteosat satellite in the IR channel at 03:00 UTC on 11 September 2011 for the IP event, **(c)** the Meteosat satellite in the IR channel at 03:00 UTC on 6 January 2011 for the ISR event, and **(d)** NOAA-18 in the thermal IR channel at 02:32 UTC on 30 January 2008 for the GEN event. The white rectangles indicate the approximate locations of the domains used in the WRF simulations.

prevailing synoptic wind. The NCEP surface analysis shows a relatively high-pressure area in the eastern Mediterranean at 00:00 UTC on 5 January, with values of around 1015 hPa, which increase to 1020 hPa at 00:00 UTC on 6 January (not shown). Another high-pressure area was located over the central Mediterranean Sea. A small and weak low-pressure area (1012 hPa) was located in southern Turkey during those days. At 850 hPa, the temperature in the eastern Mediterranean area was around 8 °C at 00:00 UTC on 5 January, and around 10 °C at 00:00 UTC on 6 January. No horizontal temperature gradient was observed in the eastern Mediterranean Sea at this height. The 10 h accumulated precipitation reached values higher than 24 mm in some parts of the rainband (see Fig. 4a).

The atmospheric dynamics producing the rainband in the GEN event, simulated by WRF-ARW (see Fig. 4b) was similar to the ISR rainband: a prevailing synoptic flow interacting with the cold inland drainage wind. The NCEP surface analysis shows two high-pressure areas located over North Africa (Tunis) and the Iberian Peninsula, with sea level pressure higher than 1030 hPa in each pressure center. A warm ridge from North Africa affected the center of the Mediterranean Basin, advecting air over the Gulf of Genoa from the southwest. At 850 hPa, the west and center of the Mediterranean Basin was affected by a relatively warm air mass,
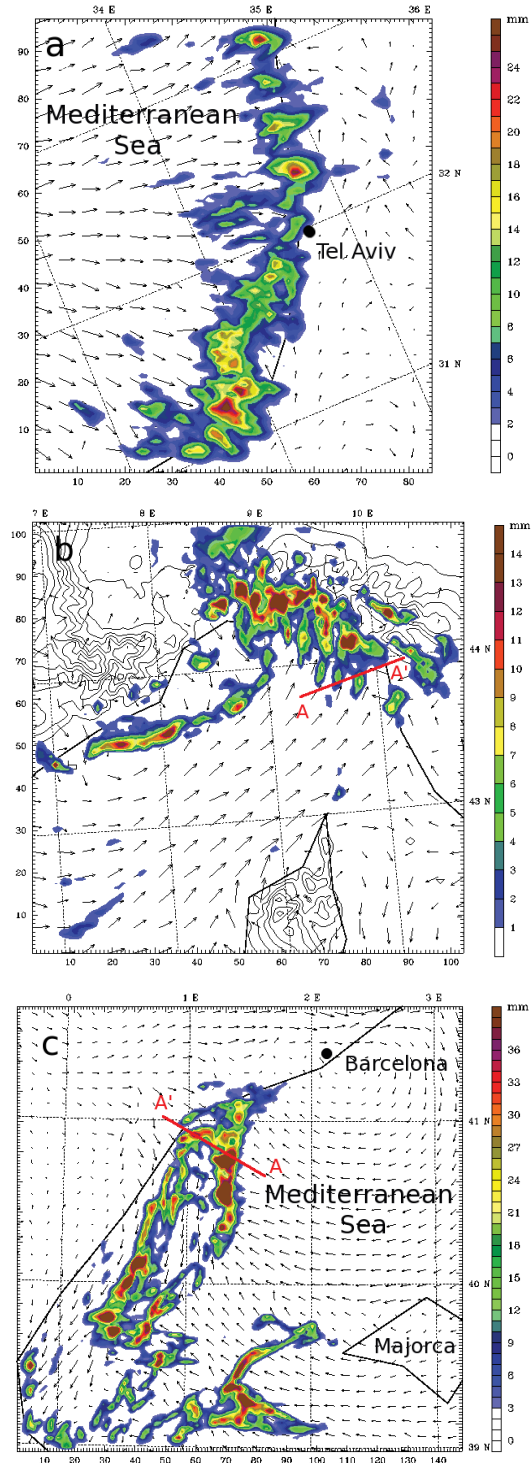

Figure 4. 10 h accumulated precipitation (color-filled contours) and surface wind field (vectors) at 10:00 UTC on **(a)** 6 January 2011 for the ISR event (maximum wind vector 6.3 m s^{-1}), **(b)** 30 January 2008 for the GEN event (maximum wind vector 11 m s^{-1}), and **(c)** 6 September 2011 for the IP event (maximum wind vector 9 m s^{-1}). In **(b)** and **(c)**, the red line AA' indicates the projection of the vertical cross section used to estimate the coastal-front depth. Note that the color scale for precipitation is not the same in the three panels.
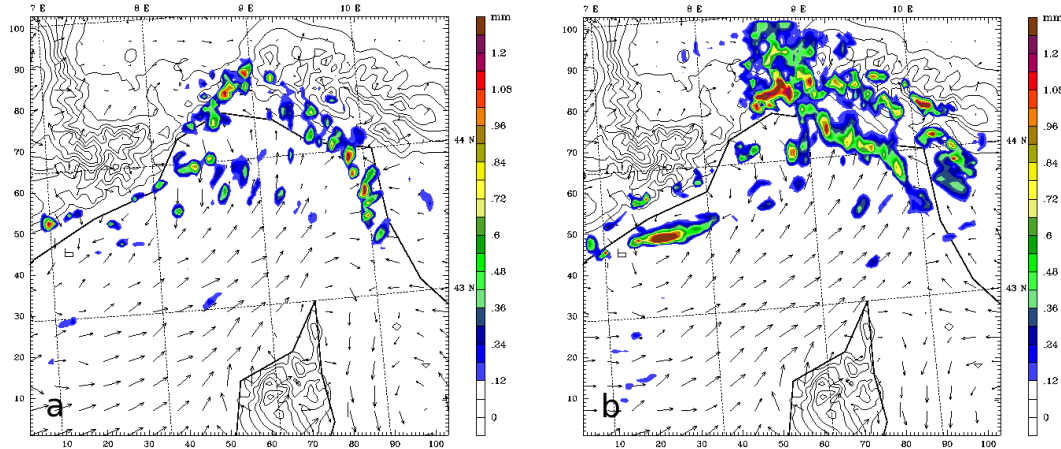
Figure 5. 1 h accumulated precipitation (color-filled contours) and surface wind field (vectors) at **(a)** 00:00 UTC (maximum wind vector 8.7 m s^{-1}) and **(b)** 06:00 UTC (maximum wind vector 9.7 m s^{-1}) on 30 January 2008 for the GEN event.

between 5 and 10°. No remarkable thermal gradients were observed over the Gulf of Genoa. In this case, the precipitation was lower than the simulated ISR precipitation, reaching a 10 h accumulated maximum value of about 14 mm.

For the IP event, the simulated rainband was produced by a non-stationary coastal front, where a convergence line moved offshore as the night progressed. Associated with this convergence line, some precipitation cells formed, producing more than 35 mm of 10 h accumulated precipitation in some parts of the rainband (see Fig. 4c).

According to the NCEP reanalysis, the synoptic situation on 5 September at 00:00 UTC was defined by a high-pressure center (1025 hPa) located over the Açores Islands, which affected the western Mediterranean Basin. However, relatively weak low pressure (1012 hPa) was located over the southern part of the Iberian Peninsula, producing a weak southeasterly flow over the east coast of the Iberian Peninsula. At a geopotential height of 850 hPa, a weak ridge from North Africa affected the southern and eastern areas of the Iberian Peninsula, with temperatures of around 15 °C at 00:00 UTC on 5 September 2011.

4.2   1 h accumulated precipitation

Figure 5 shows the simulated 1 h accumulated precipitation and surface wind field at 00:00 and 06:00 UTC for the GEN event. During this event, the WRF simulated an offshore convergence line near the coastline that extended about 100 km and remained stationary from 00:00 to 06:00 UTC (not shown). At 00:00 UTC (see Fig. 5a), several precipitation cells along the coastline were simulated at the boundary between the drainage and the prevailing synoptic flows. During the night, these cells moved onshore, but new precipitation cells formed continuously over the convergence line as shown in Fig. 5b. From 09:00 UTC, the rain bands dissipated because the wind speed of the cold air mass decreased, while

there was an increase in the parameter that accounts for the deceleration induced by the cool pool in the upstream flow.

The simulation fits well with the position of the rainband estimated by the TRMM (compare Figs. 4b and 5 with Fig. 2b) but not with the accumulated precipitation. This comparison should be taken only as qualitative, since the number of errors in both the TRMM and WRF model can be high in comparison with real values. According to the TRMM estimation, the maximum 3 h accumulated precipitation between 00:00 and 03:00 UTC was around 10 mm, while the WRF only simulated around 5 mm in the same period. Between 03:00 and 06:00 UTC, TRMM estimated less than 2 mm, while the WRF model simulated around 4 mm.

Figure 6 shows the simulated 1 h accumulated precipitation and surface wind field for the IP event at (a) 22:00 UTC on 5 September 2011, (b) 03:00, and (c) 06:00 UTC on 6 September 2011. At 22:00 UTC on 5 September 2011, some small precipitation cells were simulated over the coastline. This was triggered by the convergence at sea level between the cold air mass and the prevailing warmer easterly flow. As the cold air mass expanded along the coastline, more precipitation cells formed while it moved offshore. At 03:00 UTC (Fig. 6b) a rainband of approximately 100 km and composed of several cells was simulated offshore. The high precipitation rate simulated for this event was over 25 mm h^{-1}. The rainband moved further offshore, and at 06:00 UTC (Fig. 6c) the simulation showed an arc of precipitation of around 150 km, formed by several intense convective cells. Behind the arc, the cold air mass flow veered northwest while an easterly flow prevailed ahead of the arc. After sunrise, the wind speed of the cold air mass decreased rapidly and, by 10:00 UTC, no more precipitation cells were simulated (not shown).
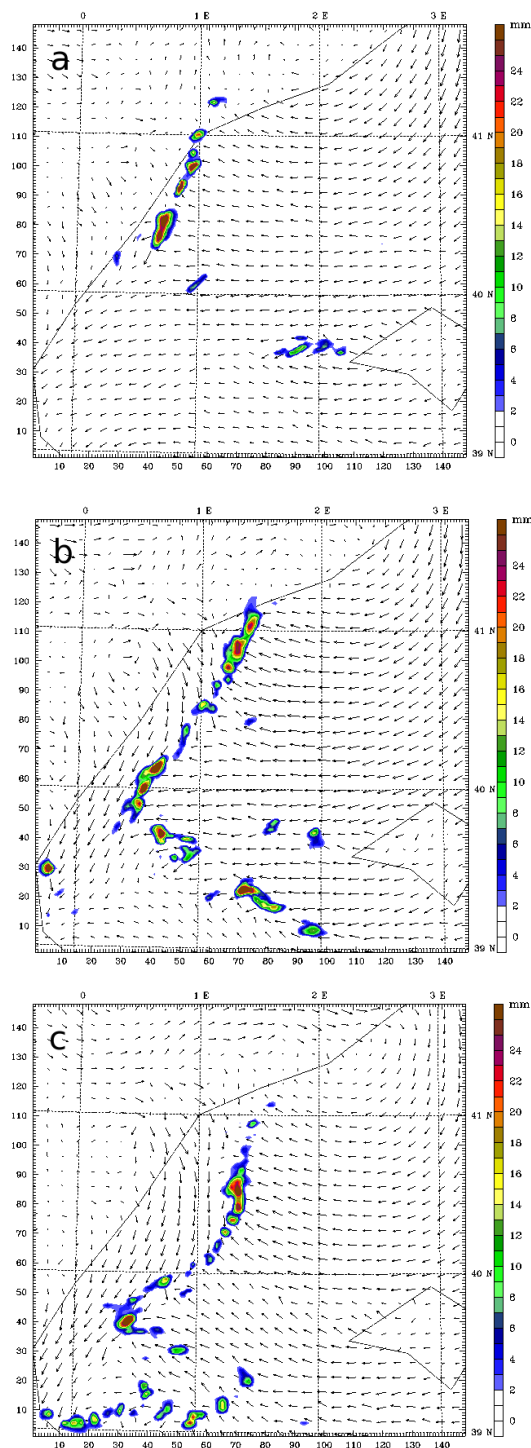
Figure 6. 1 h accumulated precipitation (color-filled contours) and surface wind field (vectors) at **(a)** 22:00 UTC (maximum wind vector 11.1 m s^{-1}) on 5 September 2011, **(b)** 03:00 UTC (maximum wind vector 9.8 m s^{-1}) and **(c)** 06:00 UTC (maximum wind vector 9 m s^{-1}) on 6 September 2011 for the IP event.

The location of the simulated rainband fit quite well with radar and Meteosat satellite observations, as well as with the TRMM estimates. At 03:00 UTC (Fig. 6b) the simulated rainband was located at approximately the same position as those recorded by the AEMET radar and Meteosat satellite, as well as that estimated by the TRMM, as shown in Figs. 3a, b and 2c, respectively. However, the WRF overestimated the TRMM values.

4.3 Physical parameters influencing rainbands

Coastal-front depth (H) plays an important role in enhancing convective precipitation by helping the warm and moist air mass reach LFC (Miglietta and Rotunno, 2010). As an example of how H is estimated by using WRF-ARM simulations, Fig. 7 shows at 03:00 UTC the vertical cross sections of potential temperature (color-filled contours), equivalent potential temperature (solid lines), wind field (vectors) and the liquid-water mixing ratio (dashed contour lines) along the AA' line that is indicated in Fig. 4b and c for the (a) GEN and (b) IP events, respectively. These dynamical structures recall a density current, whose transverse circulation is well explained (e.g., Benjamin, 1968; Simpson and Britter, 1980). The thick horizontal black line marks the height in each case where the gradient of potential temperature vanishes; H takes values of around 700 m in both events. The coastal-front depth for the ISR case is shown in Mazon and Pino (2013b), reaching around 800 m at 03:00 UTC and 1000 m at 06:00 UTC. In both Fig. 7a and b, the equivalent potential temperature decreases above the front, suggesting the presence of weak convective instability. Consequently, the relatively warm and moist lifted air mass can reach the LCL and LFC, forming convective clouds thicker than 1.4 km at 03:00 UTC as it is shown in Fig. 7. The black arrows at the bottom of these figures indicate the boundary between the cold drained air mass and the warmer maritime air mass. This is also the position where the LFC is estimated from the WRF results.

Assuming that a front acts as a mountain range blocking and lifting a prevailing warmer flow, we estimated the triggering parameter H/LFC for the three simulated nocturnal coastal fronts. Figure 8a shows the temporal evolution of H/LFC from 00:00 to 09:00 UTC for the three studied events. During most of the night for each event H/LFC > 1, indicating that convective processes were occurring over the front. Moreover, H decreased from 07:00 UTC, and shortly thereafter the triggering parameter fell to below 1, which is consistent with the decay of convection. The triggering parameter estimated from other simulated coastal fronts over the Mediterranean Basin (Mazon and Pino, 2013a, b) remained below 1 during the whole night. These events are associated with weak precipitation.

Aside from the triggering parameter H/LFC, dissipation of the rainbands is also associated with the deceleration induced by the convective cold pool in the upstream maritime
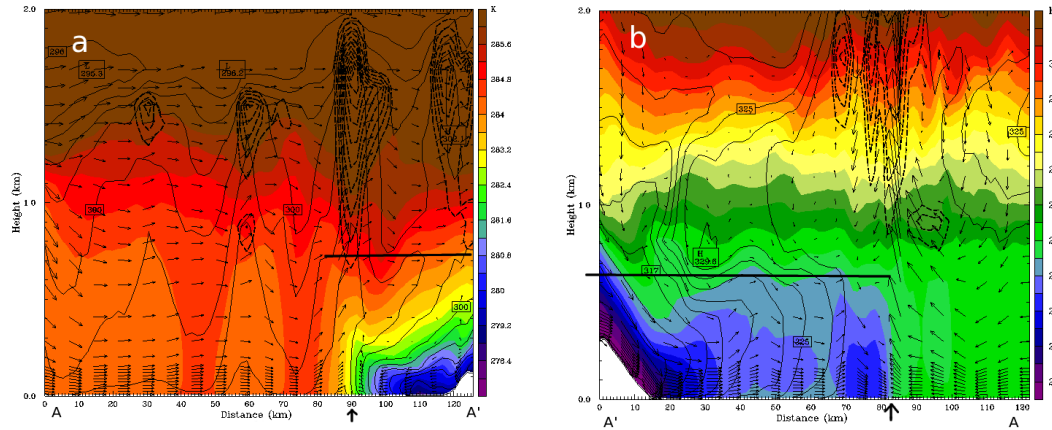
Figure 7. Vertical cross section of the potential temperature (color-filled contours), equivalent potential temperature (solid lines), liquid-water mixing ratio (dashed lines) and wind field (vectors) along the red line AA' defined in Fig. 2 at 03:00 UTC for the **(a)** GEN event (maximum horizontal wind vector $12.8\,\mathrm{m\,s^{-1}}$ and vertical $22.1\,\mathrm{cm\,s^{-1}}$) and **(b)** IP event (maximum horizontal wind vector $10.2\,\mathrm{m\,s^{-1}}$, vertical $58\,\mathrm{cm\,s^{-1}}$). The black arrow indicates the horizontal location of the front. The horizontal black line indicates the vertical location (depth) of the front. The estimated coastal-front depth, H, is about $700\,\mathrm{m}$ for both density currents, and the simulated LFC at 03:00 UTC is 582 and $650\,\mathrm{m}$ for the GEN and IP cases, respectively.

flow, as estimated by the parameter $N\mathrm{LFC}/U$ (Miglietta and Rotunno, 2010). Moreover, the reduced blockage effect of the convective cold pool on the prevailing warmer flow, is estimated by parameter NH/U (Durran and Klemp, 1987). Focusing on $N\mathrm{LFC}/U$, Fig. 8b shows its temporal evolution for the ISR, GEN, and IP events. For all cases, the estimated values for the parameter $N\mathrm{LFC}/U$ are much lower than those found by the idealized model of Miglietta and Rotunno (2010). The maximum estimated values for the three simulated rainbands occur at 09:00 UTC, suggesting that there is an upstream flow deceleration induced by the cold pool when the simulated rainbands tend to disappear. Figure 8c shows the temporal evolution of parameter NH/U from 00:00 to 09:00 UTC for the three simulated coastal fronts. The maximum value for all cases occurs between 05:00 and 07:00 UTC, when the highest values of H are estimated for the ISR, GEN and IP rainbands. This suggests that that the maximum blockage occurs around this time. Afterwards, NH/U decreases, indicating that the blockage effect is reduced.

5   Conclusions

We used satellite and reflectivity radar observations, as well as simulations of the WRF-ARW mesoscale model, to study three nocturnal coastal fronts formed by a cold inland air mass draining towards the coast and interacting with warmer, moister maritime flow. In this way, the study has contributed to a better understanding of this type of precipitation process in the Mediterranean Basin.

The simulations fit quite well with the observations, especially regarding the area of precipitation recorded by

reflectivity radar and Meteosat images for the IP and ISR events. However, in the three studied events, the TRMM values and WRF simulations show substantial differences. The TRMM estimations show a precipitation field in approximately the same region as that recorded by radar and satellite, as well as the simulated WRF, but precipitation lasts only 3 h, while in observations and simulations it lasted between 6 and 9 h. Moreover, the TRMM estimated lower 3 h accumulated values when compared with the WRF simulation for the same period in all the three cases.

Simulations show relatively high 1 and 10 h accumulated precipitation associated with the rainband cells when compared with a few other simulated events over the Mediterranean Basin. Moreover, while rainbands that formed in the GEN and ISR events were quasi-stationary, the rainband that formed during the IP event moved offshore. Regardless of the stationarity of the front, relatively large amounts of 1 and 10 h precipitation are simulated, suggesting that some other factors associated with the nocturnal coastal front contribute to producing heavy precipitation.

The investigated nocturnal coastal fronts are associated with a large convergence offshore band that is approximately parallel to the coastline where the warmer maritime air mass does not mix with the cold drained air. This large band is assumed to act as an orographic barrier. Then, using this assumption, we can define the triggering parameter (H/LFC), the deceleration parameter ($N\mathrm{LFC}/U$) and the blockage term (NH/U). In general, the evolution of these parameters behaves as expected in relation to the evolution of the simulated and observed rainbands in the three studied events.

$H/\mathrm{LFC} > 1$ is simulated for the three episodes throughout almost the entire night, when the rainbands are more developed. This suggest that the warm and moist maritime
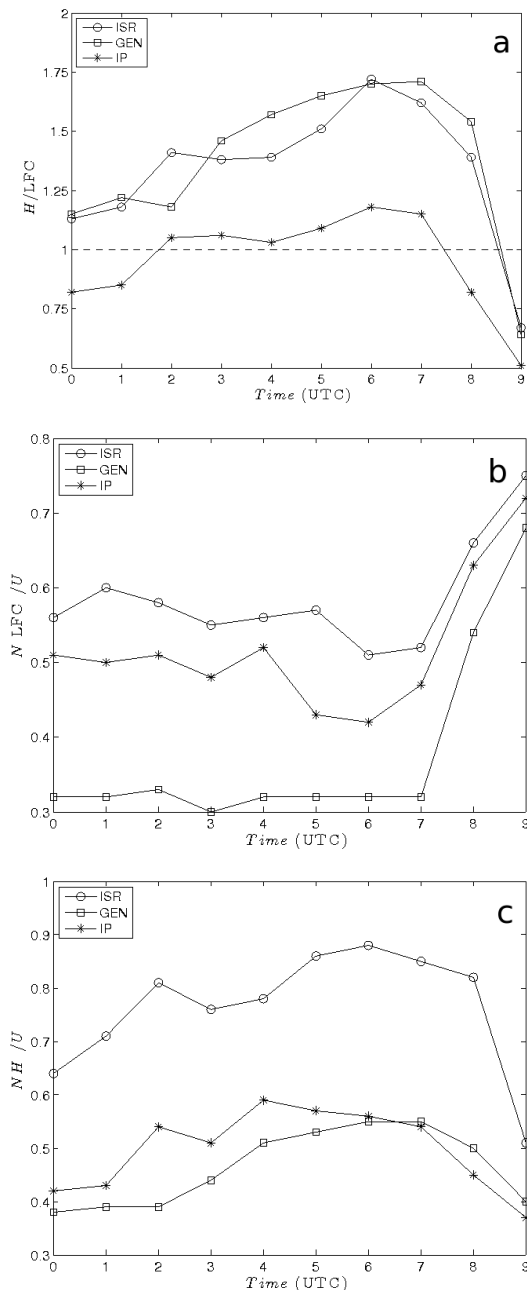
Figure 8. Temporal evolution from 00:00 to 09:00 UTC of **(a)** the triggering parameter (H/LFC), **(b)** the deceleration parameter (NLFC/U), and **(c)** the blockage parameter (NH/U) for the ISR event on 6 January 2011 (circles), GEN event on 30 January 2008 (squares) and IP event on 6 September 2011 (asterisks).

air mass reaches LFC. Maximum values are obtained between 06:00 and 08:00 UTC, when the simulated precipitation rate is higher for the IP and GEN events. From around 07:00 UTC, H decreases and LFC increases slightly for ISR and GEN events, or increases notably for IP. Consequently, the triggering parameter decreases and takes values lower than 1. In summary, if H/LFC is larger than 1, the three

simulated rainbands are well developed; while triggering parameter values lower than 1 result in dissipating rainbands.

The blockage parameter, NH/U, evolves similarly to H/LFC, with maximum values at 06:00 UTC and minimum values at the end of the night, when H decreases and the rainbands start to dissipate. At this time, the maritime air mass flows easily over the cold front. Finally, NLFC/U is approximately constant during the whole night for the two studied fronts and it increases only during the morning, because LFC increases and U decreases when the overland air temperature increases. As expected, this parameter evolves in an opposite way to the blockage parameter; i.e., if the blockage of the warm air is effective (high NH/U), the upward movement of the warm air is enhanced and the deceleration parameter consequently decreases (small NLFC/U).

Edited by: C. Ramis
Reviewed by: two anonymous referees

References

Benjamin, T. B.: Gravity currents and related phenomena, J. Fluid Mech., 31, 209–248, 1968.

Callado, A. and Pascual, R.: Storms in front of the mouth rivers in north-eastern coast of Iberian peninsula, in: Proceedings, 4th Plinius Conference on Mediterranean Storms, Mallorca, Spain, http://www.uib.es/depart/dfs/meteorologia/METEOROLOGIA/ROMU/informal/proceedings_4th_plinius_02/PDFs/Callado_and_Pascual.pdf, 2002.

Dudhia, J.: Numerical study of convection observed during the winter monsoon experiment using a mesoscale two-dimensional model, J. Atmos. Sci., 46, 3077–3107, 1989.

Durran, D. R. and Klemp, J. B.: Another look at down-slope winds, Part II: nonlinear amplification beneath wave-overturning layers, J. Atmos. Sci., 44, 3402–3412, 1987.

Frye, J. and Chen, Y.: Evolution of downslope flow under strong opposing trade winds and frequent trade-wind rainshowers over the island of Hawaii, Mon. Weather Rev., 129, 956–977, 2001.

Goldreich, Y., Mozes, H., and Rosenfeld, D.: Radar analysis of cloud system and their rainfall yield in Israel, Israel J. Earth Sci., 53, 63–76, 2004.

Grell, G. A., Dudhia, J., and Stauffer, D. R.: A description of the fifth generation Penn State/NCAR Mesoscale Model (MM5), Tech. Rep. TN-398+STR, NCAR, Boulder, CO, USA, http://nldr.library.ucar.edu/repository/assets/technotes/ TECH-NOTE-000-000-000-214.pdf, 1994.

Haddad, Z. S., Smith, E. A., Kummerow, C. D., Iguchi, T., Farrar, M. R., Durnen, S. L., Alves, M., and Olson, W. S.: The TRMM 'day-1' radar/radiometer combined rain profiling algorithm, J. Meteorol. Soc. Jpn., 75, 799–809, 1997.

Heiblum, R. H., Koren, I., and Altaratz, O.: Analyzing coastal precipitation using TRMM observations, Atmos. Chem. Phys., 11, 13201–13217, doi:10.5194/acp-11-13201-2011, 2011.

Hong, S.-H., Dudhia, J., and Chen, S.-H.: A revised approach to ice microphysical processes for the bulk parameterization of clouds and precipitation, Mon. Weather Rev., 132, 103–120, 2004.

Hong, S.-Y. and Pan, H.-L.: Nonlocal boundary layer vertical diffusion in a medium-range forecast model, Mon. Weather Rev., 124, 2322–2339, 1996.

Houze, R. A., Geostis, S. G., Marks, F. D., and West, A. K.: Winter monsoon convection in the vicinity of north Borneo, Part I: structure and time variation of the clouds and precipitation, Mon. Weather Rev., 109, 1595–1614, 1981.

Huffman, G. J., Adler, R. F., Bolvin, D. T., Gu, G., Nelkin, E. J., Bowman, K. P., Hong, Y., Stocker, E. F., and Wolff, D. B.: The TRMM multi-satellite precipitation analysis: Quasi-global, multi-year, combined-sensor precipitation estimates at fine scale, J. Hydrometeorol., 8, 38–55, 2007.

Lau, J. and Yi-Leng, C.: A case study of nocturnal rain showers over windward coastal region of the island of Hawaii, Mon. Weather Rev., 127, 2674–2692, 1999.

Mapes, B., Warner, T., Xu, M., and Negri, A.: Diurnal patterns of rainfall in northwestern South America, Part III: diurnal gravity waves and nocturnal convection offshore, Mon. Weather Rev., 131, 830–884, 2003.

Mazon, J. and Pino, D.: Pluviometric anomaly in the Llobregat delta, J. Meteorol. Clim. Mediterr., 5, 31–50, 2009.

Mazon, J. and Pino, D.: Nocturnal offshore precipitation near the Mediterranean coast of the Iberian Peninsula, Meteorol. Atmos. Phys., 120, 11–28, 2013a.

Mazon, J. and Pino, D.: The role of sea–land air thermal difference, shape of the coastline, and sea surface temperature in the nocturnal offshore convection, Tellus A, 65, 20027, doi:10.3402/tellusa.v65i0.20027, 2013b.

Miglietta, M. and Rotunno, R.: Numerical simulations of low-CAPE flows over a mountain ridge, J. Atmos. Sci., 67, 2391–2401, 2010.

Mlawer, E. J., Taubman, S.-J., Brown, P.-D., Iacono, M. J., and Clough, S. A.: Radiative transfer for inhomogeneous atmospheres: RRTM, a validated correlated-k model for the longwave, J. Geophys. Res., 102, 663–682, 1997.

Mori, S., Hamada, J., Yamanaka, M., Okamoto, N., Murata, F., Sakurai, N., Hashiguchi, H., and Sribimawati, T.: Diurnal land–sea rainfall peak and migration over Sumatra island, Indonesian maritime continent observed by TRMM satellite and intensive rawinsonde soundings, Mon. Weather Rev., 132, 2021–2039, 2004.

Murakami, M.: Analysis of the deep convective activity over the western Pacific and southeast Asia, J. Meteorol. Soc. Jpn., 61, 60–75, 1983.

Neumann, J.: Land breezes and nocturnal thunderstorms, J. Meteorol., 8, 60–67, 1951.

Ohsawa, T., Ueda, H., Hayashi, T., Watanabe, A., and Masumoto, J.: Diurnal variations of convective activity and rainfall in tropical Asia, J. Meteorol. Soc. Jpn., 79, 333–352, 2003.

Schoenberg, L. M.: Doppler radar observation of land–breeze cold front, Geophys. Res. Lett., 112, 2455–2464, 1984.

Simpson, J. E. and Britter, R. E.: A laboratory model of atmospheric mesofront, Q. J. Roy. Meteorol. Soc., 106, 485–500, 1980.

Skamarock, W. C., Klemp, J. B., Dudhia, J., Gill, D. O., Barker, D. M., Duda, M., Huang, X.-Y., and Powers, J. G.: A Description of the Advanced Research WRF Version 3, Tech. Rep. TN-475+STR, NCAR, Boulder, CO, USA, 2008.

Wapler, K. and Lane, T.: A case of offshore convective initiation by interacting land breezes near Darwin, Australia, Meteorol. Atmos. Phys., 5, 123–137, 2012.

Wu, P., Yamanaka, M., and Matsumoto, J.: The formation of nocturnal rainfall offshore from convection over western Kalimantan (Borneo) island, J. Meteorol. Soc. Jpn., 86A, 187–203, 2008.

Yu, C. and Jou, B.: Radar observations of the diurnal forced offshore convection lines among the southeastern coast of Taiwan, Mon. Weather Rev., 133, 1613–1636, 2004.